Magnetic coupling of guest metallocene molecules with SURMOF-2 host matrix

Alexei Nefedov [1,*] Chun Li,[1] Kai Müller [1] Anemar Bruno Kanj [1] Lars Heinke [1] Chen Luo [2] Kai Chen [2]
Florin Radu [2] Evangelos Golias [3] Wolfgang Kuch [3] and Christof Wöll [1]

[1]*Karlsruhe Institute of Technology, Institute of Functional Interfaces, Hermann-von-Helmholtz-Platz 1,*
76344 Eggenstein-Leopoldshafen, Germany
[2]*Helmholtz-Zentrum Berlin für Materialen und Energie, Albert-Einstein-Straße 15, 12489 Berlin, Germany*
[3]*Freie Universität Berlin, Institut für Experimentalphysik, Arnimallee 14, 14195 Berlin, Germany*

Metal-organic frameworks (MOFs) are crystalline and porous, molecular solids consisting of metal nodes and organic ligands. An interesting example is the MOF-2 system, where Cu^{2+} ions form antiferromagnetically coupled dimers to yield so-called paddlewheels. In the case of surface-anchored MOF-2 (SURMOF-2) systems the Cu^{2+} ions are connected via carboxylate and OH groups in a zipperlike fashion. This unusual coupling of the spin-1/2 ions within the resulting one-dimensional chains stabilizes a low-temperature ferromagnetic (FM) phase. In this study, the magnetic properties of two SURMOF-2 systems (Cu(bdc) and Cu(bpdc) with bdc = 1, 4-benzendicarboxylic acid, bpdc = 4,4-biphenyldicarboxylic acid) were investigated using x-ray magnetic circular dichroism both in the absorption and in the scattering geometry. The presence of the FM phase in these SURMOF-2 systems is confirmed. Taking advantage of the element sensitivity of this technique. it was established that the magnetic signal originates from Cu^{2+} ions. After loading of SURMOF-2 with metallocene molecules, no remarkable changes of the magnetic properties of the host matrix were observed. However, the magnetic behavior of the guest molecules, as it turned out, is rather different. In the case of nickelocene loading, a polarization effect was found, resulting in ferromagnetic ordering of the guest molecules. However, in the case of manganocene derivatives, the polarization effect is not observed and these molecules remained in their paramagnetic state. The details of these effects are discussed.

I. INTRODUCTION

Metal–organic frameworks (MOFs), also known as porous coordination polymers (PCPs), are crystalline, molecular solids that have emerged in the last three decades as a family of novel materials. The common property of all these crystalline frameworks, constructed from the assembly of inorganic subunits (metal nodes) and organic linkers, is their high permanent porosity [1,2]. The porosity, in combination with other unique properties, like the enormous variety and flexibility, makes MOFs suitable for various applications, for example, the storage and separation of small molecules [3] as well as a greenhouse gas sequestration [4]. In addition the presence of inorganic subunits has led to applications in heterogeneous catalysis [5,6] as well as in conductivity [7–9] and magnetism [8–12]. Moreover, the presence of magnetic centers either in the nodes or in the pores of a crystalline MOF allows to create organized magnetic nanostructures, while keeping them well separated in space. Such a feature may be of potential interest in quantum technologies, since there a controlled disposition of magnetic moieties in space is required. And, a recent study of the quasilinear metal-ion chains suggested that this easy-to-fabricate class of materials exhibits interesting one-dimensional (1D) magnetic properties [13].

Surface-anchored MOFs (SURMOFs) are oriented, highly crystalline thin films of MOFs [14,15], which are grown by liquid-phase (quasi)-epitaxy in a well-defined step-by-step mode on a functionalized substrate. For our study we used a particular class of SURMOFs, denoted as SURMOF 2 [Figs. 1(a) and 1(b)], which is derived from MOF 2, one of the simplest framework architectures [16,17]. MOF-2 is based on paddlewheel (pw) units formed by attaching 4 dicarboxylate moieties to Cu^{2+} or Zn^{2+} dimers, yielding planar sheets with fourfold symmetry. These planes are held together by strong carboxylate–metal bonds [18]. Conventional solvothermal synthesis yields a stack of pw planes shifted relative to each other, with a corresponding reduction in symmetry to yield a P2 or C2 structure [16,19,20]. The motivation for the present work is based on results of Friedländer *et al.*, who have recently reported the ferromagnetic ordering in the Cu(bdc)/Cu(bpdc) (bdc = 1, 4-benzendicarboxylic acid, bpdc = 4,4-biphenyldicarboxylic acid) SURMOF-2 series with Curie temperatures around 20 K [21]. It is important to note that, in contrast to other 1D systems, no strong magnetic fields are needed to induce a sizable magnetization.

A growing number of experiments using atom and shell selectivity of synchrotron radiation techniques are carried out to study magnetic properties. In this context, x-ray magnetic circular dichroism (XMCD) spectroscopy is a powerful technique that measures the difference in absorption of left- and right-circularly polarized x rays by a magnetized sample, often at cryogenic temperatures. By now XMCD

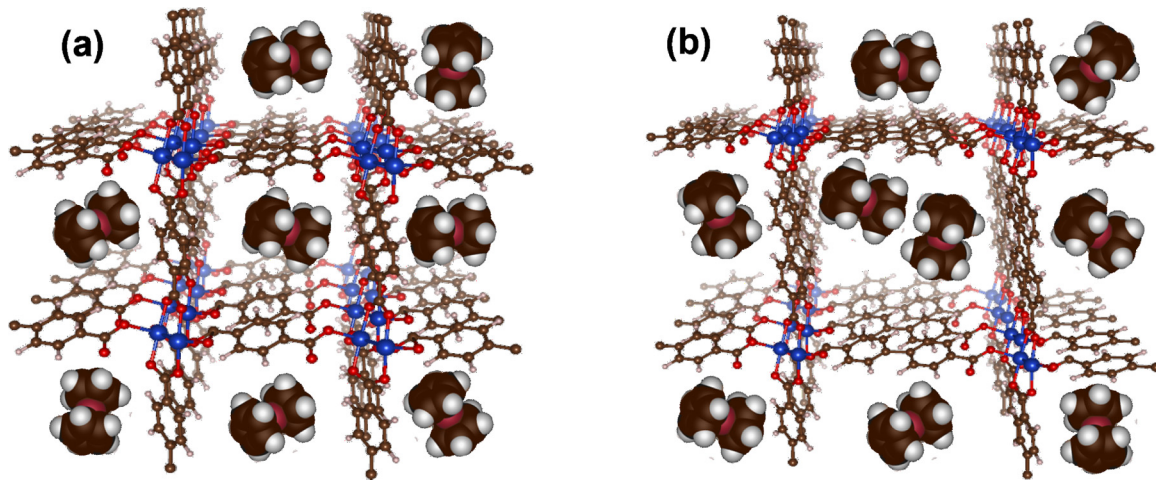*Corresponding author: alexei.nefedov@kit.edu

FIG. 1. Cu(bdc) (a) and Cu(bpdc) (b) SURMOF-2 structures (blue: copper, red: oxygen, brown: carbon, white: hydrogen). The zipperlike chain of Cu^{2+} is presented; Metallocene molecules: brown, carbon: white, hydrogen: magenta Me (Ni, Mn). Sketches of the host matrix and guest molecules are presented only for illustration.

is well established in magnetic materials science, and has also become an important tool for the investigation of both (metallo)organic [22] and (bio)inorganic [23] samples. As with all x-ray absorption spectroscopies (XAS), XMCD has the advantage of being element specific, i.e., it allows to separate different magnetic components in heterogeneous samples [24]. X-ray resonant magnetic scattering (XRMS), which is XMCD in the scattering geometry, uses the energy dependence of corrective terms to the atomic scattering factor being sensitive to the magnetization of the sample [25,26]. This method is very useful to study magnetic thin films, heterostructures, and multilayers, including a determination of magnetic order or disorder on the interfaces (magnetic roughness) and interlayer coupling. In order to study XMCD and XRMS in $3d$ transition metals, experiments are conveniently carried out over their $L_{3,2}$ absorption edges, which are placed in the soft x-ray range and special vacuum conditions are required. With new synchrotron radiation sources and improved end stations, XMCD/XRMS measurements on heterogeneous samples are becoming more routine.

The aim of the current study was to shed more light on magnetic coupling of the metallocenes with the Cu magnetic moments in Cu(bdc)/Cu(bpdc) systems [Figs. 1(a) and 1(b)]. For that, the metallocene guest molecules were loaded into the pores of the SURMOF-2 host. Subsequently, the magnetic behavior of both the empty host frame and host/guest system have been investigated. We have chosen nickelocene and manganocene derivative – nickelocene – bis(cyclopentadienyl)nickel, manganocene derivative – bis(isopropyl-cyclopentadienyl)manganese) for a loading in Cu(bdc)/Cu(bpdc) surface-anchored frameworks. This manganocene derivative is below referred to as manganocene*. The choice of possible guest molecules is limited, because other metallocenes are either very sensitive to air and unstable (vanadocene, cobaltocene) or do not exhibit any magnetic moment (ferrocene). The additional interest to use manganocene derivatives in the study is based both on possible steric effect and on the observation of a high-spin electron configuration in such compounds [27].

II. EXPERIMENT

A. Sample preparation

Before the SURMOF synthesis, the gold substrate (100-nm Au/5-nm TiO_2 deposited on Si wafer) was functionalized by a carboxylic acid-terminated self-assembled monolayer (SAM) [28]. To this end, the substrate was immersed in a 20 μM ethanolic solution of 16-mercaptohexadecanoic acid for about 2 days. Then, the Cu(bdc) and Cu(bpdc) SURMOF-2 films (bdc = 1, 4-benzendicarboxylic acid, bpdc = 4,4-biphenyldicarboxylic acid) have been grown at room temperature in a step-by-step fashion using spray-coating process [29–31]. The substrates were placed on the sample holder and subsequently sprayed with 1 mM copper acetate $(Cu_2(CH_3COO)_4 \cdot H_2O)$ ethanolic solution for 10 s and with 0.2 mM of bdc or 0.1 mM of bpdc ethanolic solutions for 20 s, respectively. In between these two steps there was a break of 30 s, during which the sample was cleaned by rinsing with pure ethanol. Each cycle was repeated 50 times. The total thickness of the SURMOF films amounted to about 100 nm.

The loading with nickelocene and manganocene* was performed from the liquid phase. The SURMOFs were immersed for 4 h in the ethanolic nickelocene and manganocene* solutions with a concentration of 17 and 24 mg per ml, respectively. The concentrations amounted to approximately 10% of the saturation concentration. To avoid oxygen and air exposure, the solution preparation and SURMOF loading were done in an oxygen-free nitrogen glovebox.

The crystallinity of the SURMOF samples was investigated with x-ray diffraction (XRD), using x-ray radiation of $\lambda = 0.15419$ nm (Cu $K\alpha_{1,2}$ radiation). The x-ray diffractograms (Fig. S1 in the Supplemental Material (SM) [32]) show clear diffraction peaks in full agreement with the calculated structures, verifying a high degree of crystallinity with the SURMOF-2 structures as described previously [15].

B. XMCD/XRMS experiments

The XMCD/XRMS experiments were performed at the high-field end station VEKMAG [33] installed at the dipole

beamline PM2 of the synchrotron facility BESSY II, which is operated by the Helmholtz-Zentrum Berlin (HZB). This end station offers unique capabilities for this type of research, since it provides a vector magnetic field with a maximum magnetic field up to 9 T in the beam direction, 2 T in the horizontal plane, and 1 T in all directions for a temperature range of 2–500 K. The temperature calibration was done by using a calibrated Cernox sensor that was mounted on a sample holder. The base pressure in the end station at room temperature was 2×10^{-10} mbar.

The x-ray absorption spectra were recorded by means of total electron yield, measuring the drain current as a function of the photon energy. Measured signals were normalized by a Ta grid x-ray monitor mounted in a magnetically shielded environment as the last optical element before the sample. During the XAS/XMCD measurements, the magnetic field was applied collinear with the photon beam; the sample was oriented both in grazing ($\theta = 20°$, in-plane magnetization) and in normal (out-of-plane magnetization) incidence geometry. The following normalization procedure of x-ray absorption spectra was used—first, the linear preedge background is subtracted; second, the rest intensity is normalized to the intensity of the L_3 peak.

XRMS measurements were carried out both in θ-2θ mode around the (001) reflection keeping the photon energy of the synchrotron radiation at the Cu L_3 edge as well as at the fixed incidence angle while varying the photon energy. A Si photodiode has been used as a detector of the scattered beam. XMCD/XRMS were measured with fixed helicity and alternating magnetic field $B = \pm 8$ T parallel to the incoming beam. The degree of circular polarization is $P = 0.77$.

In order to get an acceptable signal-to-noise ratio for the magnetization curves the following procedure was applied: First, for every value of the magnetic field, XMCD spectra were acquired five times at the energies of the Cu (Ni, Mn) L_3 and L_2 peaks, which were determined from corresponding wide-range XAS/XMCD scans. Then, after averaging, the magnetic contrast ($I^+ - I^-$) was normalized to the intensities of the corresponding XAS $L_{3,2}$ peaks ($I^+ + I^-$). Since for all magnetization curves no differences in the data measured both during the increase and during the decrease of the magnetic field were observed (no visible hysteresis), the measured data were additionally averaged. In order to get stable temperature conditions, the samples were first cooled down to the lowest possible temperature, and then they were kept at these conditions up to 2 h. The XMCD/XRMS measurements were started only after the temperature had stabilized. For most of the measurements the temperature, based on the calibration, was 8.4 K. For temperature-dependent experiments, an additional radiation shield was installed, resulting in a lowest temperature of 3 K.

In order to determine whether the x-ray beam does not damage the sample structure (reduction of Cu^{2+} ion to a nonmagnetic Cu^+ state) or/and no possible water adsorption/growth of ice layer takes place, XAS data have been measured twice, before and after rather long series of magnetization curves. Fortunately, even after several hours of measurements we did not detect any changes in the x-ray absorption spectra. We thus conclude that under the experimental conditions used here both radiation damage and water adsorption were absent or negligible.

III. RESULTS AND DISCUSSION

A. Pristine SURMOF-2 samples

X-ray absorption Cu $L_{3,2}$ edge spectra (($I^+ + I^-$)/2) and the corresponding XMCD signals ($I^+ - I^-$) measured for the Cu(bdc) and Cu(bpdc) SURMOF-2 samples in the grazing-incidence geometry are presented in Figs. 2(a) and 2(b), respectively. Both XAS measurements look very similar with two pronounced peaks at photon energies of 931.1 and 950.9 eV, corresponding to the $L_{3,2}$ edges of Cu^{2+}. These XAS spectra are almost identical to the XAS spectra of CuO presented in the paper of Kvashnina *et al.* [34]. The ground state in this case can be also described as a mixture of $3d^9$ and $3d^{10}\underline{L}$ character [35], where $\underline{L}$ stands for a hole in the O $2p$ band. The main peak at 931.1 eV corresponds to the $2p^5 3d^{10}$ final state. This state gives a single line without multiplet splitting, because the d shell is filled. At ~ 20 eV above this peak ($2p_{3/2}$), another structure with lower intensity appears ($2p_{1/2}$). This structure is broader due to a shorter core-hole lifetime and interaction with the $2p_{3/2}$ continuum [34]. Cu $L_{3,2}$ XAS data and corresponding XMCD signal obtained for normal-incidence geometry are presented in Figs. S2(a) and S2(b) in the Supplemental Material (SM) [32]. No feature corresponding to Cu^+ at around 933.5 and 953.4 eV was observed for all spectra, confirming the absence of SURMOF-2 degradation under the synchrotron radiation. The XMCD signals (red-filled areas) look typical, demonstrating rather strong magnetic contribution in x-ray absorption spectra for all samples. The ferromagnetic behavior is clearly seen for all magnetization curves ([Figs. 2(c) and 2(d) and S2(c) and S2(d)] in SM [32]) with some paramagnetic contribution, which is more pronounced for Cu(bpdc) measured at the normal-incidence geometry. Additionally, rather small, but clearly visible anisotropy (easy axis parallel to the surface) was observed in full accordance with previous results of Friedländer *et al.* [21].

In a next step, the magnetic properties of Cu(bdc) SURMOF-2 were investigated in dependence on the sample temperature. As mentioned above, a special thermoshield was additionally installed to reach temperatures less than 8 K. Because of the design of this shield, XAS/XMCD experiments could be carried out in the normal-incidence geometry only and, therefore, the presented data were obtained for the out-of-plane magnetization. First, the sample was cooled down to 3 K at zero magnetic field. After temperature stabilization, XMCD measurements were carried out around the Cu L_3 edge with the reswitching of the direction of the magnetic field, which was varied from 0.5 to 4 T. Then, the sample temperature was increased and, after its stabilization, the measurements were carried out again. This procedure was repeated for temperatures in the range of 3–50 K. The obtained data are presented in Fig. 3. They are in very good agreement with similar measurements by superconducting quantum interference device reported in Ref. [21]. The steplike shape of the curves proves ferromagnetic behavior; the different height of the saturation of the XMCD signal towards low temperatures for different
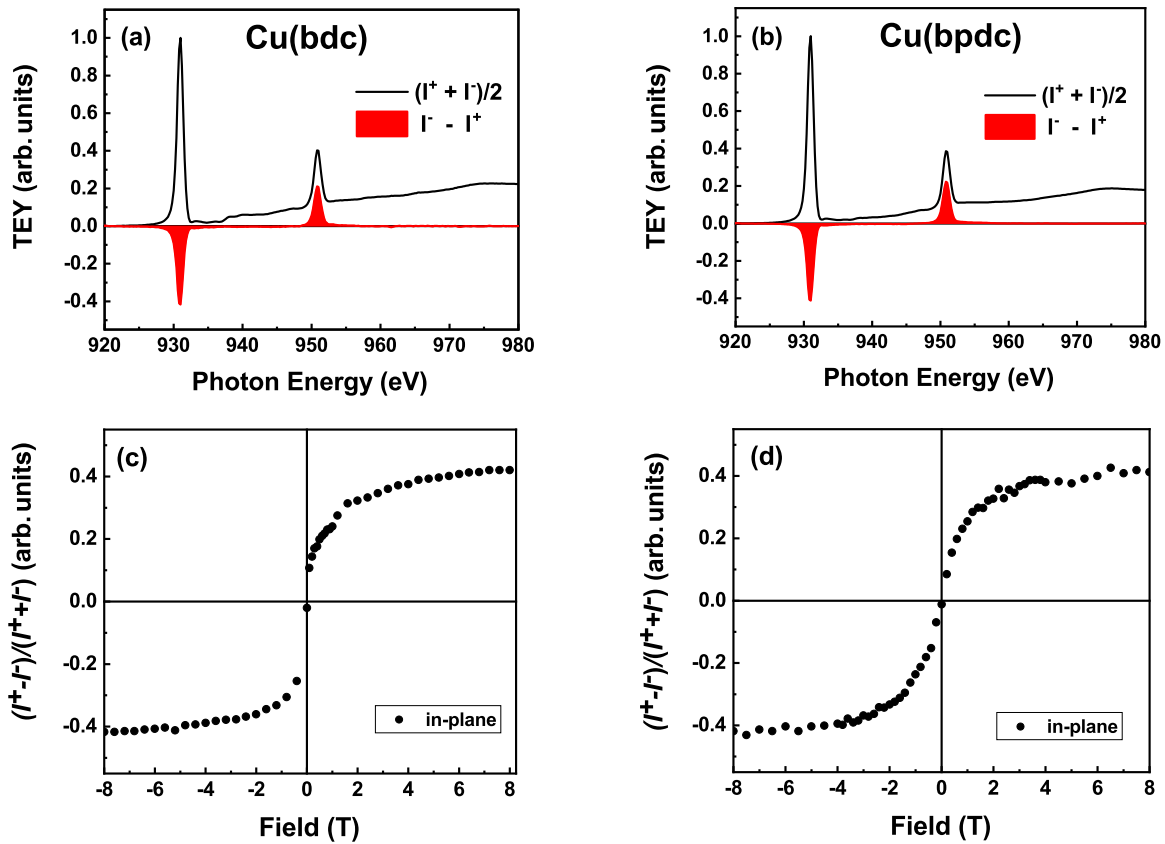
FIG. 2. X-ray absorption spectra $[(I^+ + I^-)/2$, black lines] and corresponding XMCD signals ($I^+ - I^-$, red-filled areas) measured on the Cu $L_{3,2}$ edges of Cu(bdc) (a) and Cu(bpdc) (b) SURMOF-2 in the grazing-incidence geometry. The magnetic field during the measurements was ± 8 T, pointing parallel to the incident beam. Magnetization curves $(I^+ + I^-)/(I^+ - I^-)$ of Cu(bdc) (c) and Cu(bpdc) (d) SURMOF-2 measured at $T = 8.4$ K for in-plane magnetization.

fields indicates the presence of some secondary antiferromagnetic interactions, as discussed in Ref. [21].

B. X-ray resonant magnetic scattering

As mentioned above, SURMOFs are highly oriented crystalline thin films with high structural quality. Since the unit-cell size amounts to about 1 nm, it is possible to observe Bragg peaks not only with hard x-ray diffraction (Fig. S1 in SM [32]), but in the soft x-ray range as well. Moreover, with
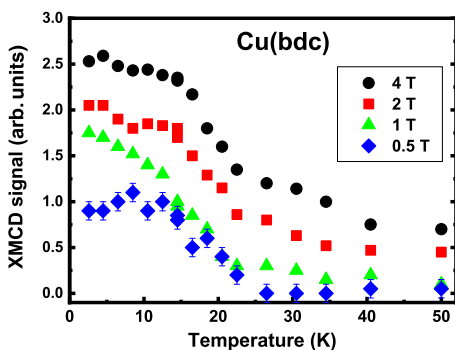

FIG. 3. Temperature dependence of the XMCD signal measured at normal incidence on Cu(bdc) SURMOF-2 film.

the use of circular-polarized radiation with a photon energy corresponding to an absorption edge, the magnetic contribution in scattering intensity can be detected as well [26]. The Cu(bpdc)(100) Bragg peak, measured in $\theta/2\theta$ mode at the fixed photon energy corresponding to the maximum of the Cu L_3 edge, is presented in Fig. 4(a). In Fig. 4(b) the same Bragg peak was measured at fixed $\theta/2\theta$ angle positions while varying the photon energy around the Cu L_3 edge. The magnetic field was set to ± 8 T. The magnetic contrast is clearly visible here as well.

As it was mentioned above, the XRMS technique suited well for the study of magnetic multilayers and a determination of a possible interlayer (ferromagnetic or antiferromagnetic) coupling in such systems. This opportunity is rather unique, because such kind of coupling cannot be recognized from XMCD measurements in a straightforward way. Surface-anchored MOFs grown by the step-by-step method with magnetic Cu^{2+} chains could be considered as magnetic multilayer as well, and interlayer coupling could be expected. In the case of antiferromagnetic coupling, the magnetic period will be doubled and the so-called half-order peak should be observed. In order to check for such an antiferromagnetic coupling between neighboring Cu^{2+} chains, the photon energy was fixed at $E = 931.1$ eV (Cu L_3 edge) and XRMS measurements around the position of the half-order peak ($\theta \sim 13°$) were carried out, but no additional features were observed in the measured spectra.
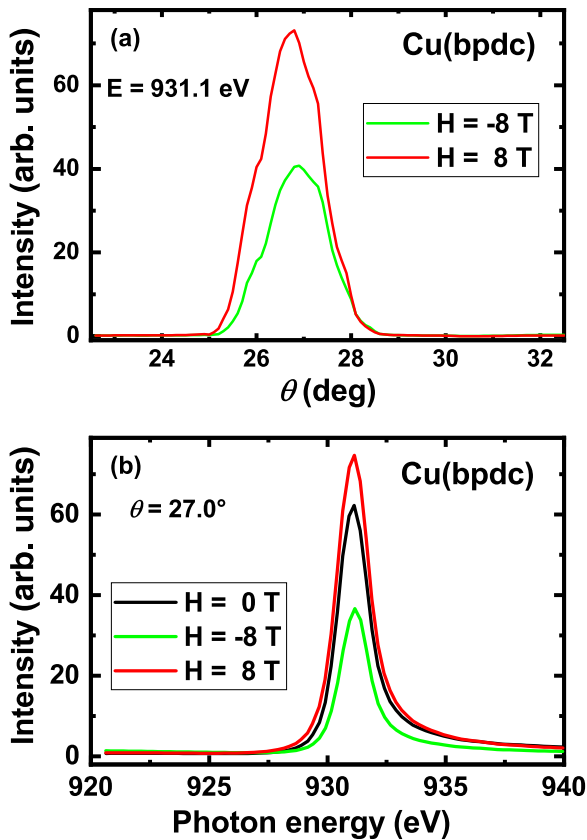
FIG. 4. Cu(bpdc)(100) Bragg peak measured: (a) in $\theta/2\theta$ mode at the fixed photon energy corresponding to the maximum of the Cu L_3 edge and (b) at fixed $\theta/2\theta$ angle positions while varying the photon energy around this absorption edge. The black curve was measured at zero field, the red and green curves at 8 and -8 T, correspondingly.

To summarize this part of our study, we have successfully demonstrated the applicability of XMCD/XRMS techniques for the investigation of the magnetic properties of SURMOF-2 systems. Both for Cu(bdc) and Cu(bpdc) the magnetic behavior is very similar and no dependence of the magnetic behavior on the chain-chain distance in SURMOF-2 systems has been observed. This observation strongly suggests that a ferromagnetic coupling between two neighboring chains is absent and, on the basis of XRMS results, antiferromagnetic coupling between these chains could be also excluded. Our results directly confirm the statements made by Friedländer *et al.* that such systems could be considered as 1D magnet [21].

C. Metallocene-loaded SURMOF-2 samples

Since in empty SURMOF-2 systems there is no magnetic coupling between the chains formed by the Cu^{2+} ions, it was decided to check whether such a coupling can be induced by loading the pores of the SURMOFs with magnetic metallocene guest molecules, namely nickelocene and manganocene*. In the latter case it was interesting to check also for a possible effect of the presence of additional isopropyl groups on the behavior of the guest molecules in the host SURMOF-2 structure.

Cu $L_{3,2}$ edge x-ray absorption spectra and corresponding XMCD signal measured on nickelocene-loaded Cu(bdc) in the grazing-incidence geometry are presented in Fig. 5(a). The XAS/XMCD data look very similar to the spectra measured on unloaded SURMOF-2 sample [Fig. 2(a)]. In Fig. 5(b), x-ray absorption spectra and corresponding XMCD signals measured on the Ni $L_{3,2}$ edges for this sample are presented as well. The XAS/XMCD data obtained for nickelocene-loaded Cu(bpdc) in the grazing-incidence geometry both for Cu- and Ni $L_{3,2}$ edges are presented in Figs. S3(a) and S3(b) in the Supplemental Material [32]. All data obtained in the normal-incidence geometry for both SURMOF-2 systems are presented in Figs. S5 and S6 in SM [32]. In all Ni $L_{3,2}$ spectra, in addition to the main peaks at photon energies of 852.7 and 870.0 eV corresponding to a Ni $L_{3,2}$-edges splitting of $\sim$17 eV, a fine structure is observed. Such a fine structure is typical for a $3d^8$ configuration of Ni^{2+} as it was calculated for such ion in bis(diphenylbis((methylthio)- methyl)borate)nickel [36].

The XMCD signal of Ni [red-filled area in Fig. 5(b)] demonstrates a sizable magnetic contribution from the guest molecules. The small positive XMCD signal at $E = 854.9$ eV originates possibly from a partly occupied d_z^2 orbital. In this case it has an opposite sign with respect to the XMCD signal at 852.7 eV, similar to observations of Arruda *et al.* for Co porphyrins adsorbed on a Cu(100) substrate [37]. However, since the spectra do not change considerably with the incidence angle, this would then imply that the Ni quantization axes (in respect to the d_z^2 orbitals) lie in different directions in different molecules according to our suppositions.

In Figs. 5(c) and 5(d) we present the magnetization curves (in-plane magnetization) of nickelocene-loaded Cu(bdc) measured at the Cu- and the Ni $L_{3,2}$ edges, respectively. The shape of the magnetization curve measured at the Cu $L_{3,2}$ edges [Fig. 5(c)] clearly demonstrates the ferromagnetic behavior. Its shape is almost the same as for the empty samples [Fig. 2(c)]. The magnetization curve measured at the Ni $L_{3,2}$ edges [Fig. 5(d)] demonstrates a magnetic behavior of the guest molecules as well. In spite of pure paramagnetic properties of nickelocene in the solid phase [38], here the presence of both ferromagnetic and paramagnetic contributions in the magnetic signal is clearly seen. We explain this behavior with a polarization of some part of the guest molecules from ferromagnetically ordered Cu^{2+} chains, keeping the rest of the molecules in unpolarized paramagnetic state. No reasonable magnetic anisotropy was observed in this case that allows us to conclude about an absence of any ordered configuration of the nickelocene molecules in the SURMOF-2 host system.

To get more information about the magnetic properties of this system, we analyze the field-dependent XMCD data of Ni-loaded Cu(bdc). In a first step, we model the field-dependent XMCD of the Cu $L_{3,2}$ edges [Fig. 5(c)], using a simple mean-field approximation for purely ferromagnetic coupling between Cu magnetic moments. The following assumptions are made: $S = 1/2$ (then there is no anisotropy in zero-field splitting), identical ferromagnetic interactions between all Cu atoms, neglecting any antiferromagnetic interactions as well as additional coupling across the Ni atoms, $T = 8.4$ K (see Supplemental Material [32] for further details). The black curve is the best fit, which was obtained for a parameter of $T_C = 8.7$ K. The only other fit parameter is a
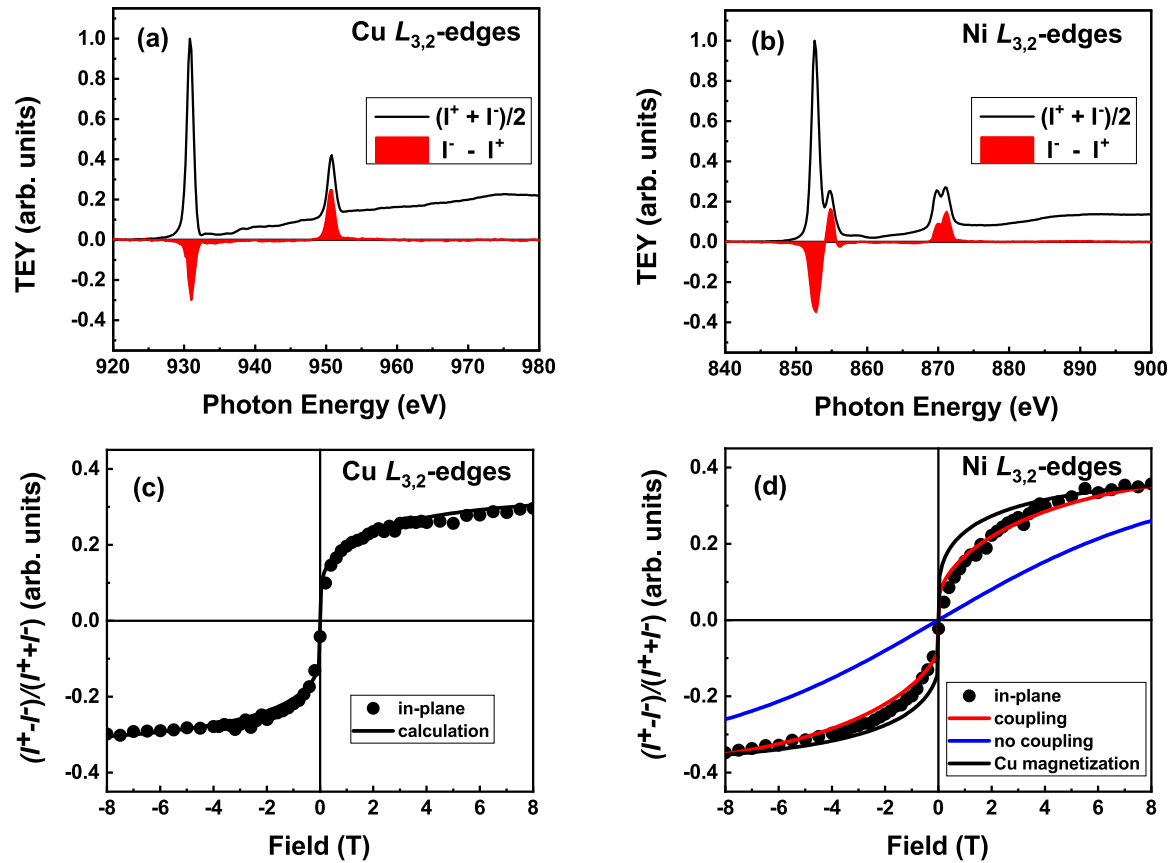
FIG. 5. X-ray absorption spectra $(I^+ + I^-)/2$ (black lines) measured at Cu (a) and Ni $L_{3,2}$ edges (b) on nickelocene-loaded Cu(bdc) samples in the grazing-incidence geometry. The corresponding XMCD signals $I^+ - I^-$ are shown as red-filled area. Magnetic field during the XMCD measurements was ± 8 T, parallel to the incident beam. Magnetization curves (points) of nickelocene-loaded Cu(bdc) measured at the Cu $L_{3,2}$ edges (c) and the Ni $L_{3,2}$ edges (d). The black curves in (c), (d) are the calculation using mean-field approximation for ferromagnetic coupling between Cu magnetic moments. The red curve in (d) is a fit by a simple model taking into account the coupling between Cu and Ni ions (for details see the text). Pure paramagnetic behavior of the Ni ions is presented by the blue curve (d).

factor used to match the experimental XMCD signal to the simulation. The good agreement between experimental and calculated data is clearly seen in spite of some asymmetry of the experimental data around ± 2 T. We can also convert this T_C value into a coupling energy J_{Cu} using $J_{Cu} = 3k_B/n_{NN} \cdot T_C$ (still neglecting the role of nickelocene for that), n_{NN} is the number of nearest Cu-neighbor atoms. Since there are 2 Cu nearest neighbors, we obtain $J_{Cu} = 1.1$ meV.

In the next step we use this simulated curve, representing the Cu $L_{3,2}$ edge XMCD data, and compare it to the Ni $L_{3,2}$ edge XMCD data [Fig. 5(d)]. A very rough approximation to estimate the coupling energy of individual Ni atoms is applied: coupling to the average Cu magnetization as contribution to the effective field for the Ni moments [39] and identical coupling strength for all nickelocenes. For details see the Supplemental Material [32]. The black curve in [Fig. 5(d)] is the same as on [Fig. 5(c)] with a small rescaling only; it is used as the average Cu magnetization in the model. From the deviation of the Ni data from that curve it is seen that the coupling energy must be of about the same order as $k_B T$. Assumptions made for the Ni data are $S = 1$, $\mu = 2\,\mu_B$, $T = 8.4$ K, no anisotropy. The red curve is now a fit of this simple model to the experimental data points, using the vertical scaling and the coupling energy $J_{Ni} = 0.7$ meV as fit parame-

ters. Paramagnetic moments, in contrast, would yield the blue curve. If paramagnetic excess nickelocene molecules were present in the sample, the coupling energy of the coupled nickelocenes would be accordingly higher. It seems that the Ni-Cu coupling is a direct double-exchange coupling, with a coupling strength of the same order as the Cu-Cu coupling J_{Cu}.

In order to investigate the possible proximity effect, we used manganocene* (bis(isopropyl-cyclopentadienyl) manganese), in which two hydrogen atoms were substituted with two isopropyl groups. In this situation the presence of these groups does not allow guest molecules to come very close to Cu^{2+} chains and thus any polarization induced by a direct contact should be absent.

To clarify this point, the Cu $L_{3,2}$ XAS spectrum (black line) and corresponding XMCD signal (red-filled area) measured on manganocene*-loaded Cu(bdc) in the grazing-incidence geometry are presented in Fig. 6(a). Both XAS spectrum and XMCD signal look almost the same as for the pristine SURMOF-2 films. X-ray absorption spectra and corresponding XMCD signal measured on the Mn $L_{3,2}$ edges for these samples are presented as well [Fig. 6(b)]. The XAS/XMCD data obtained for the Mn-cene*-loaded Cu(bpdc) SURMOF-2 film are presented in Figs. S4(a) and S4(b) in the SM [32]. In the XAS spectrum, in addition to the L_3 main peak at a
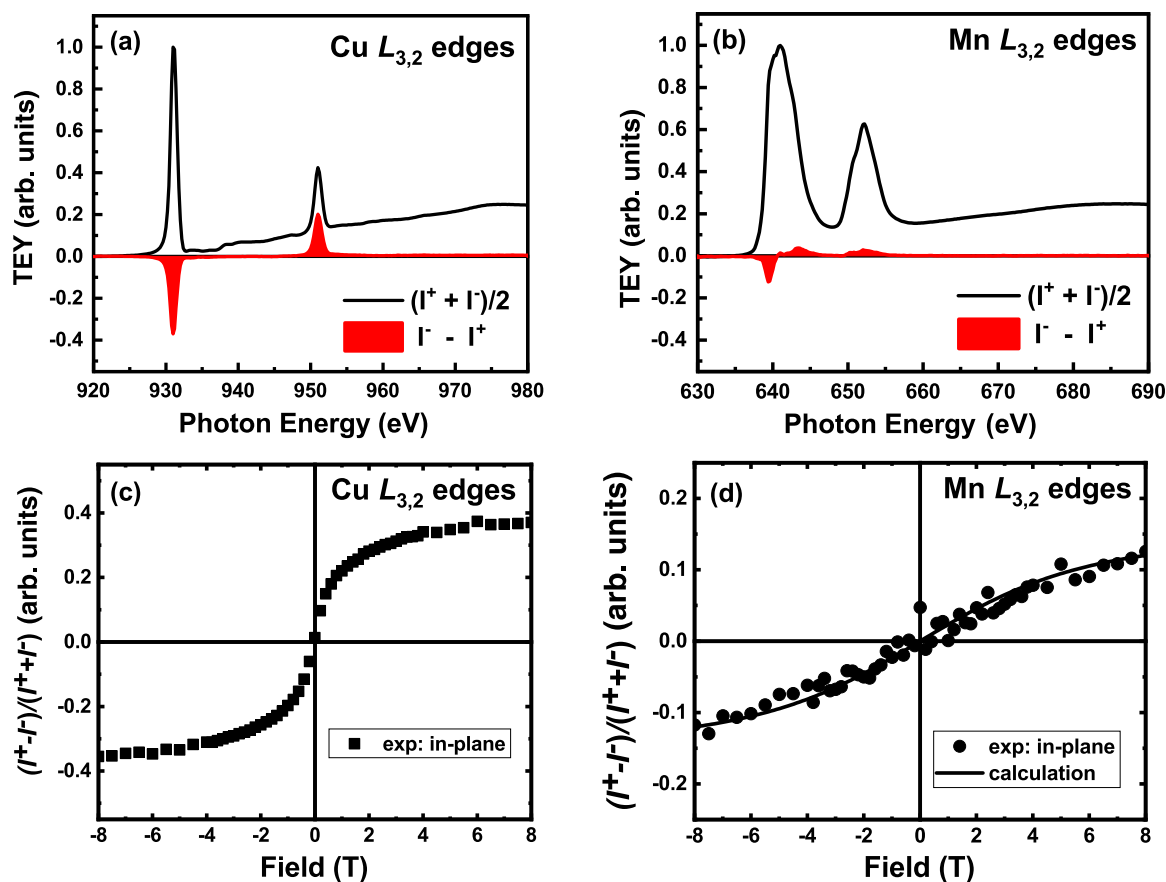
FIG. 6. X-ray absorption spectra $(I^+ + I^-)/2$ (black lines) measured at the Cu $L_{3,2}$ edges (a) and the Mn $L_{3,2}$ edges (b) on Cu(bdc) in the grazing-incidence geometry. The corresponding XMCD signals $I^+ - I^-$ are shown as red-filled area. The magnetic field during the XMCD measurements was ± 8 T, parallel to the incident beam. Magnetization curves of Mn*-loaded Cu(bdc) measured at in-plane (black points) magnetization at $T = 8.4$ K. Experimental curves were measured at the Cu $L_{3,2}$ edges (c) and the Mn $L_{3,2}$ edges (d). Solid line in (d) is an isotropic Brillouin function ($T = 8.4$ K, $S = 2$; the vertical scaling was chosen to fit the calculated curve with the corresponding experimental data).

photon energy of 639.1 eV, two less-resolved satellites are observed and the L_2 peak has a doubletlike structure. Such a fine structure is typical for a Mn^{2+} state ($3d^5$ configuration) [40], which is also expected for manganocene*. The rather broad line shape of the L_3 peak could be explained with a formation of Mn^{2+}-Mn^{2+} dimers [40] or an oxidation of manganese to the Mn^{3+} state [41]. The XMCD signal at the Mn $L_{3,2}$ edges (red-filled areas) is also clearly visible, but the intensity is much lower in comparison to the one at the Ni $L_{3,2}$ edges in nickelocene-loaded samples. XAS/XMCD data measured in the normal-incidence geometry as well as corresponding magnetization curves look very similar (see Figs. S7 and S8 in Supplemental Material [32]).

The magnetization curves of manganocene*-loaded SURMOF-2 samples have been measured in in-plane/out-of-plane magnetization at $T = 8.4$ K as well. In Fig. 6(c) we present the magnetization curve acquired at the Cu $L_{3,2}$ edges for Cu(bdc). The ferromagnetic behavior is clearly seen for the curve measured at the Cu $L_{3,2}$ edges with some paramagnetic contribution. The shape of the curve is almost the same as for the pristine (empty) samples [Fig. 2(c)]. The magnetization curve measured at the Mn $L_{3,2}$ edges [Fig. 6(d)] demonstrates substantially different magnetic behavior of these guest

molecules. While in the case of nickelocene, the main part of the guest molecules was ferromagnetically aligned with the Cu moments, for manganocene*, the magnetic signal is paramagnetic. To confirm this statement, we compared the experimental Mn XMCD magnetization data with an isotropic Brillouin function (calculated for 8.4 K and $S = 2$ [solid line in Fig. 6(d)]; see Supplemental Material [32] for further details. Although the Brillouin function shows already some curvature at this temperature, it is compatible with the experimental data, considering a different vertical scaling. This behavior could be explained with the absence of any polarization from ferromagnetically ordered Cu^{2+} chains, which could be explained either by the internal electronic structure of manganocene* or, more probably, the presence of the substituted isopropyl groups. In the latter case these groups could prevent an opportunity for Mn^{2+} centers to be placed close to Cu^{2+} chains and to be polarized.

Summarizing our observations, we conclude that the guest molecules do not change the magnetic ordering of Cu^{2+} chains in the SURMOF-2 host. Moreover, nickelocene molecules are polarized themselves from the ferromagnetically ordered Cu^{2+} ions. These effects could be explained with a proximity effect, i.e., only those molecules which are placed

close to the Cu^{2+} chains could be polarized. In the case of manganocene*, no polarization was observed at all.

IV. CONCLUSIONS

In conclusion, the magnetic properties of the SURMOF-2 systems Cu(bdc) and Cu(bpdc) were investigated using x-ray magnetic circular dichroism both in the absorption and in the scattering geometry. The presence of the FM phase in these SURMOF-2 systems has been confirmed. Taking advantage of the element sensitivity of this technique it was directly established that the magnetic signal originates from Cu^{2+} ions. For both SURMOF-2 films, Cu(bdc) and Cu(bpdc), the magnetic behavior is very similar and no dependence on the chain-chain distance in these systems has been observed. It means that a ferromagnetic coupling between two neighboring chains is absent and, on the basis of XRMS results, antiferromagnetic coupling between these chains could be also excluded. After loading of SURMOF-2 with metallocene molecules, a different behavior of magnetic properties was found. In the case of nickelocene loading a polarization effect was found, resulting in ferromagnetic alignment of the guest molecules. However, the polarization effect was not observed in the case of manganocene derivatives and the molecules remain paramagnetic. It seems that the Ni-Cu coupling is a direct double-exchange coupling, while the coupling between Cu-Mn is absent.

[1] H.-C. Zhou, J. R. Long, and O. M. Yaghi, Introduction to metal–organic frameworks, Chem. Rev. **112**, 673 (2012).

[2] M. Eddaoudi, J. Kim, N. Rosi, D. Vodak, J. Wachter, M. O'Keeffe, and O. M. Yaghi, Systematic design of pore size and functionality in isoreticular MOFs and their application in methane storage, Science **295**, 469 (2002).

[3] M. T. Kapelewski, T. Runčevski, J. D. Tarver, H. Z. H. Jiang, K. E. Hurst, P. A. Parilla, A. Ayala, T. Gennett, S. A. FitzGerald, C. M. Brown, and J. R. Long, Record high hydrogen storage capacity in the metal–organic framework $Ni_2(m\text{-}dobdc)$ at near-ambient temperatures, Chem. Mater. **30**, 8179 (2018).

[4] M. Ding, R. W. Flaig, H. L. Jiang, and O. M. Yaghi, Carbon capture and conversion using metal–organic frameworks and MOF-based materials, Chem. Soc. Rev. **48**, 2783 (2019).

[5] M. Ranocchiari and J. A. Van Bokhoven, Catalysis by metal–organic frameworks: Fundamentals and opportunities, Phys. Chem. Chem. Phys. **13**, 6388 (2011).

[6] A. Dhakshinamoorthy, Z. Li, and H. Garcia, Catalysis and photocatalysis by metal organic frameworks, Chem. Soc. Rev. **47**, 8134 (2018).

[7] L. Sun, M. G. Campbell, and M. Dinc, Electrically conductive porous metal-organic frameworks, Angew. Chem., Int. Ed. **55**, 3566 (2016).

[8] K. Siemensmeyer, C. A. Peeples, P. Tholen, F.-J. Schmitt, B. Çoşut, G. Hanna, and G. Yücesan, Phosphonate metal–organic frameworks: A novel family of semiconductors, Adv. Mater. **32**, 2000474 (2020).

[9] C. Yang, R. Dong, M. Wang, P. S. Petkov, Z. Zhang, M. Wang, P. Han, M. Ballabio, S. A. Bräuninger, Z. Liao *et al.*, A semiconducting layered metal-organic framework magnet, Nat. Commun. **10**, 3260 (2019).

[10] E. Coronado and G. Mínguez Espallargas, Dynamic magnetic MOFs, Chem. Soc. Rev. **42**, 1525 (2013).

[11] G. Mínguez Espallargas and E. Coronado, Magnetic functionalities in MOFs: From the framework to the pore, Chem. Soc. Rev. **47**, 533 (2018).

[12] E. Coronado, M. Giménez-Marqués, G. Mínguez Espallargas, and L. Brammer, Tuning the magneto-structural properties of non-porous coordination polymers by HCl chemisorption, Nat. Commun. **3**, 828 (2012).

[13] E. D. Bloch, W. L. Queen, R. Krishna, J. M. Zadrozny, C. M. Brown, and J. R. Long, Hydrocarbon separations in a metal-organic framework with open iron(II) coordination sites, Science **335**, 1606 (2012).

[14] O. Shekhah, J. Liu, R. A. Fischer, and C. Wöll, MOF thin films: Existing and future applications, Chem. Soc. Rev. **40**, 1081 (2011).

[15] J. Liu, B. Lukose, O. Shekhah, H. K. Arslan, P. Weidler, H. Gliemann, S. Bräse, S. Grosjean, A. Godt, X. Feng *et al.*, A novel series of isoreticular metal organic frameworks: Realizing metastable structures by liquid phase epitaxy, Sci. Rep. **2**, 921 (2012).

[16] H. Li, M. Eddaoudi, T. L. Groy, and O. M. Yaghi, Establishing microporosity in open metal-organic frameworks: Gas sorption isotherms for Zn(BDC) (BDC = 1,4-Benzenedicarboxylate), J. Am. Chem. Soc. **120**, 8571 (1998).

[17] U. Mueller, M. Schubert, F. Teich, H. Puetter, K. Schierle-Arndt, and J. Pastré, Metal-organic frameworks - prospective industrial applications, J. Mater. Chem. **16**, 626 (2006).

[18] O. Shekhah, H. Wang, D. Zacher, R. A. Fischer, and C. Wöll, Growth mechanism of metal-organic frameworks: Insights into the nucleation by employing a step-by-step route, Angew. Chem. Int. Ed. **48**, 5038 (2009).

[19] C. G. Carson, K. Hardcastle, J. Schwartz, X. Liu, C. Hoffmann, R. A. Gerhardt, and R. Tannenbaum, Synthesis and structure characterization of copper terephthalate metal-organic frameworks, Eur. J. Inorg. Chem. **2009**, 2338 (2009).

[20] H. F. Clausen, R. D. Poulsen, A. D. Bond, M. A. S. Chevallier, and B. B. Iversen, Solvothermal synthesis of new metal organic framework structures in the zinc-terephthalic acid-dimethyl formamide system, J. Solid State Chem. **178**, 3342 (2005).

[21] S. Friedländer, J. Liu, M. Addicoat, P. Petkov, N. Vankova, R. Rüger, A. Kuc, W. Guo, W. Zhou, B. Lukose *et al.*,

Linear chains of magnetic ions stacked with variable distance: Ferromagnetic ordering with a Curie temperature above 20 K, Angew. Chem. Int. Ed. **55**, 12683 (2016).

[22] Y. Bodenthin, G. Schwarz, Z. Tomkowicz, A. Nefedov, M. Lommel, H. Möhwald, W. Haase, D. G. Kurth, and U. Pietsch, Structure-driven remanent high-spin state in metallo-supramolecular assemblies, Phys. Rev. B **76**, 064422 (2007).

[23] T. Funk, A. Deb, S. J. George, H. Wang, and S. P. Cramer, X-ray magnetic circular dichroism—a high energy probe of magnetic properties, Coord. Chem. Rev. **249**, 3 (2005).

[24] J. Grabis, A. Bergmann, A. Nefedov, K. Westerholt, and H. Zabel, Element-specific x-ray circular magnetic dichroism of Co$_2$ Mn Ge Heusler thin films, Phys. Rev. B **72**, 024437 (2005).

[25] A. Nefedov, J. Grabis, A. Bergmann, K. Westerholt, and H. Zabel, Soft x-ray resonant magnetic scattering studies on Co$_2$ Mn Ge Heusler films, Physica B **345**, 250 (2004).

[26] J. Grabis, A. Bergmann, A. Nefedov, K. Westerholt, and H. Zabel, Element-specific characterization of the interface magnetism in [Co$_2$MnGe/Au]$_n$ multilayers by x-ray resonant magnetic scattering, Phys. Rev. B **72**, 024438 (2005).

[27] H. Sitzmann, M. Schär, E. Dormann, and M. Kelemen, High spin-Manganocene mit sperrigen, alkylierten Cyclopentadienyl-Liganden, Z. Anorg. Allg. Chem. **623**, 1609 (1997).

[28] M. Kind and C. Wöll, Organic surfaces exposed by self-assembled organothiol monolayers: Preparation, characterization, and application, Prog. Surf. Sci. **84**, 230 (2009).

[29] L. Heinke and C. Wöll, Surface-mounted metal–organic frameworks: Crystalline and porous molecular assemblies for fundamental insights and advanced applications, Adv. Mater. **31**, 1806324 (2019).

[30] H. K. Arslan, O. Shekhah, J. Wohlgemuth, M. Franzreb, R. A. Fischer, and C. Wöll, High-throughput fabrication of uniform and homogenous MOF coatings, Adv. Funct. Mater. **21**, 4228 (2011).

[31] S. Hurrle, S. Friebe, J. Wohlgemuth, C. Wöll, J. Caro, and L. Heinke, Sprayable, large-area metal–organic framework films and membranes of varying thickness, Chem. A Eur. J. **23**, 2294 (2017).

[32] See Supplemental Material at http://link.aps.org/supplemental/10.1103/PhysRevB.107.054433 for additional experimental data.

[33] T. Noll and F. Radu, *Proceedings of the 9th Mechanical Engineering Design of Synchrotron Radiation Equipment and Instrumentation (MEDSI2016)* (JACoW, Geneva, Switzerland, 2017), p. 370.

[34] K. O. Kvashnina, S. M. Butorin, A. Modin, I. Soroka, M. Marcellini, J-H. Guo, L. Werme, and J. Nordgren, Changes in electronic structure of copper films in aqueous solutions, J. Phys.: Condens. Matter **19**, 226002 (2007).

[35] A. S. Koster, X-ray Lα emission and L$_{III}$ absorption spectra of copper compounds, Mol. Phys. **26**, 625 (1973).

[36] H. Wang, C. Y. Ralston, D. S. Patil, R. M. Jones, W. Gu, M. Verhagen, M. Adams, P. Ge, C. Riordan, C. A. Marganian *et al.*, Nickel L-edge soft x-ray spectroscopy of nickel-iron hydrogenases and model compounds - evidence for high-spin Nickel(II) in the active enzyme, J. Am. Chem. Soc. **122**, 10544 (2000).

[37] L. M. Arruda, Md. E. Ali, M. Bernien, N. Hatter, F. Nickel, L. Kipgen, C. F. Hermanns, T. Bißwanger, P. Loche, B. W. Heinrich *et al.*, Surface-orientation- and ligand-dependent quenching of the spin magnetic moment of Co porphyrins adsorbed on Cu substrates, Phys. Chem. Chem. Phys. **22**, 12688 (2020).

[38] M. Sorai, Y. Kaneko, and T. Hashiguchi, Heat capacity of paramagnetic nickelocene: Comparison with diamagnetic ferrocene, J. Phys. Chem. Solids **75**, 656 (2014).

[39] M. Bernien, J. Miguel, C. Weis, Md. E. Ali, J. Kurde, B. Krumme, P. M. Panchmatia, B. Sanyal, M. Piantek, P. Srivastava *et al.*, Tailoring the Nature of Magnetic Coupling of Fe-Porphyrin Molecules to Ferromagnetic Substrates, Phys. Rev. Lett. **102**, 047202 (2009).

[40] M. M. Grush, J. Chen, T. L. Stemmler, S. J. George, C. Y. Ralston, R. T. Stibrany, A. Gelasco, G. Christou, S. M. Gorun, J. E. Penner-Hahn, and S. P. Cramer, Manganese L-edge x-ray absorption spectroscopy of manganese catalase from lactobacillus plantarum and mixed valence manganese complexes, J. Am. Chem. Soc. **118**, 65 (1996).

[41] V. Bayer, R. Podloucky, and C. Franchini, F. Allegretti, B. Xu, G. Parteder, M. G. Ramsey, S. Surnev, and F. P. Netzer, Formation of Mn$_3$O$_4$ (001) on MnO(001): Surface and interface structural stability, Phys. Rev. B **76**, 165428 (2007).